Latin American Journal of Solids and Structures
www.lajss.org

Effect of Thermal Treatment on the Dynamic Behaviors at a Fixed Loading Rate of Limestone in Quasi-vacuum and Air-filled Environments

Abstract

Thermal damage in rock engineering occurs in the air-filled and quasi-vacuum environments of rock mass located near or far from the free surface. Meanwhile, dynamic loads are encountered frequently in engineering practice. In this study, 39 limestone samples are prepared, and a series of laboratory tests, including split Hopkinson pressure bar (SHPB), nuclear magnetic resonance (NMR) and optical microscopy analyses, are conducted to investigate the effects of temperature and the environment on the dynamic mechanical properties of limestone. The results show that the macro-physical and dynamic mechanical properties of limestone after thermal treatment can be divided into two stages by a critical temperature of 450°C, at which the thermal damage factor is 0.71 and 0.75 in the quasi-vacuum and air-filled environments, respectively. In the first stage, with temperatures varying from 25°C to 450°C, the thermal damage due to expansion and fracturing slightly influences the related parameters, except the P-wave velocity. However, in the second stage, with temperatures ranging from 450°C to 900°C, the thermal damage caused by mineral decomposition and hydration leads to a remarkable decrease in the dynamic bearing and anti-deformation capacities. The environment plays a negligible role in the first stage but an important role in the second stage, and the dynamic compressive strength and modulus of samples after thermal treatment in the air-filled environment are much lower than those in the quasi-vacuum environment. Both the temperature and environment of thermal treatment should be considered in engineering practice, especially when the temperature exceeds 450°C.

Keywords

Thermal damage; Environment; Dynamic mechanical behaviors; SHPB; NMR; limestone

Liyuan Yu [a]
Haijian Su [a]
Richeng Liu [a*]
Hongwen Jing [a]
Guanglei Li [a]
Ming Li [a]

[a] State Key Laboratory for Geomechanics and Deep Underground Engineering, China University of Mining and Technology, Xuzhou 221116, PR China. E-mail: liuricheng@cumt.edu.cn, yuliyuan@cumt.edu.cn, hjsu@cumt.edu.cn, liuricheng@cumt.edu.cn, hwjingcumt@163.com, 751208714@qq.com, mingl@cumt.edu.cn

*Corresponding author

http://dx.doi.org/10.1590/1679-78254021

Received: May 13, 2017
In Revised Form: December 20, 2017
Accepted: January 10, 2018
Available online: February 05, 2018

1 INTRODUCTION

Thermal effects are important environmental factors in rock engineering procedures, including rock drilling, ore crushing, deep petroleum boring, geothermal energy extraction, deep burial of nuclear waste (Heuze 1983), underground post-disaster reconstruction (Han et al. 2012) and underground coal gasification (Kapusta et al. 2013). These effects have interested many researchers because thermal treatments influence the physical (David et al. 1999; Vinciguerra et al. 2005; Chaki et al. 2008; Nara et al. 2011; Ozguven and Ozcelik 2014) and static mechanical properties (Ferrero and Marini 2001; Balme et al. 2004; Koca et al. 2006; Heap et al. 2009; Brotóns et al. 2013) of rocks. In addition, rock dynamics must be considered in earthquake, mining, energy, environmental and civil engineering studies when dynamic loads are encountered, such as during explosions (Roy et al. 2016; Yu et al. 2017), impacts (Wang et al. 2009), seismic events (Grana and Rossa 2010) and microseismic events (Dai et al., 2016a, 2017). The split Hopkinson pressure bar (SHPB) system, which is the only dynamic device recommended (Zhou et al. 2012) by the International Society for Rock Mechanics (ISRM), has been widely used to conduct dynamic compression tests (Frew et al. 2001), dynamic Brazilian tests (Wang et al. 2009; Dai et al. 2008, 2010) and dynamic notched semi-circular bend tests (Chen et al. 2009; Dai et al. 2016b) at a high strain rate ($10^2 \sim 10^3$ s^{-1}).

(cc) BY

Thermal treatments firstly influence the physical properties of rocks such as density, P-wave velocity, porosity, permeability, water absorption, heat conductivity and so on. Ozguven and Ozcelik (2014) reported that bulk density of limestone and marble decreases dramatically with the increase in temperature, especially after 400°C. This is caused by the capillary cracks that occur in natural stones, expansion and materials left from the structure. Nasseri et al. (2007) believed that both the number and average opening distance of microcracks increase after the thermal treatment (up to 850°C) for Westerly granite. Xu et al. (2008) reported that granite remains stable at temperatures below 800°C and that its carrying capacity is destroyed at approximately 1200°C. Sengun (2014) measured the elastic modulus by heating the carbonate of six different material components to 600°C, reporting a reduction of 62% ~ 82%. Recently, a few scholars have investigated the effects of thermal treatment on the dynamic mechanical properties of rocks. Liu and Xu (2014) declared that the growth factor of dynamic compressive strength of Qinling biotite exhibits a continuous uptrend with increasing temperature, and reaches its maximum at 1000°C. Yin et al. (2015) reported that the dynamic tensile strength of granite increases with temperature up to 100°C, while it quickly decreases as temperature exceeds 100°C. X-ray Micro-computed tomography (CT) technique was utilized to quantify the damage of Longyou sandstone induced by the thermal treatment, then the dynamic compressive (Huang and Xia 2015) and tensile (Yao et al. 2016) strengths were obtained using the SHPB system under different dynamic loading rates. Li et al. (2016) reported that the dynamic mechanical properties of coal measures sandstone rapidly weaken due to the decomposition of kaolinite when the temperature exceeds 500°C. Based on the test data of heattreated granite specimens(up to 900°C), the dynamic behavior and failure characteristics of the granite under the coupling action of temperature and impact loading were studied by Wang and Hao (2017).

However, thermal damage to rock masses due to rock engineering occurs in different environments and different regions. Rocks near the free surface will be heated in an air-filled environment (AE) with various gases and moisture in the atmosphere, while rocks far from the free surface will be heated in a quasi-vacuum environment (QE) that lacks gases and moisture. Thermal treatments, such as tunnel fires (Li and Ingason 2013; Gong et al. 2016) and underground coal gasification (Bhutto et al. 2013), occur more frequently in the QE occurs than in the AE. In this study, limestone samples were collected from both the QE and AE after thermal treatment and prepared with temperatures ranging from 25°C to 900°C. Then, the macro-physical and dynamic mechanical parameters of these samples were measured via a series of tests, in which the effects of thermal treatment were investigated.

2 TESTS

2.1 Basic properties of limestone and sample preparation

A dark grey limestone is chosen in this study to demonstrate the influence of thermal treatment on its dynamic mechanical behavior under uniaxial compression. This type of limestone is mainly composed of calcite (96%) and small amounts of dolomite (2%), montmorillonite (1%) and illite (1%) based on the results of X-ray diffraction (XRD). A non-destructible method, X-ray computed tomography (CT), was used to verify the homogeneity of a typical sample. The Xradia MicroXCT-400 system provides a high-resolution scan with a 120 W X-ray source of 148 kV. Figure 1a shows CT images at four equidistant cross-sections, and each scanned image consists of 2048 × 2048 pixels with a resolution of 30 μm. The grey level, which provides a visual representation of the material density (Raynaud et al. 1989), displays good consistency between the four CT images.

The static mechanical behavior of a natural state sample (Φ50 mm × 100 mm) was obtained via a uniaxial compression test, as shown in Figure 1b. The physical and static mechanical parameters are listed in Table 1. A post-peak falling stage in the stress-strain curve and the splitting failure mode reflect the hard brittle characteristics of this limestone sample.

In the dynamic compressive test using the SHPB, 50-mm diameter cores were drilled into the limestone. These cores were then cut into cylinders with a height of 50 mm for an appropriate aspect ratio ($L/D = 1$), as recommended by the ISRM (Zhou et al. 2012). The precision control of samples was performed in accordance with the standard requirements of the ISRM (Ulusay and Hudson 2007), with parallelism controlled within $\pm$0.05 mm and surface flatness within $\pm$0.02 mm.

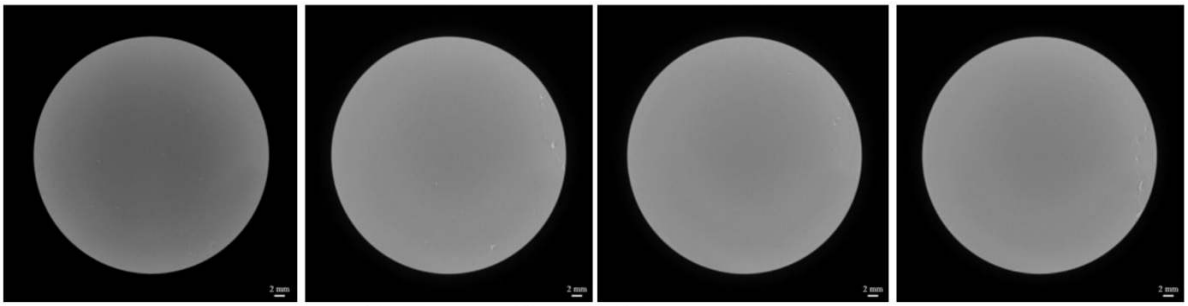

(a) CT images of four equidistant cross-sections

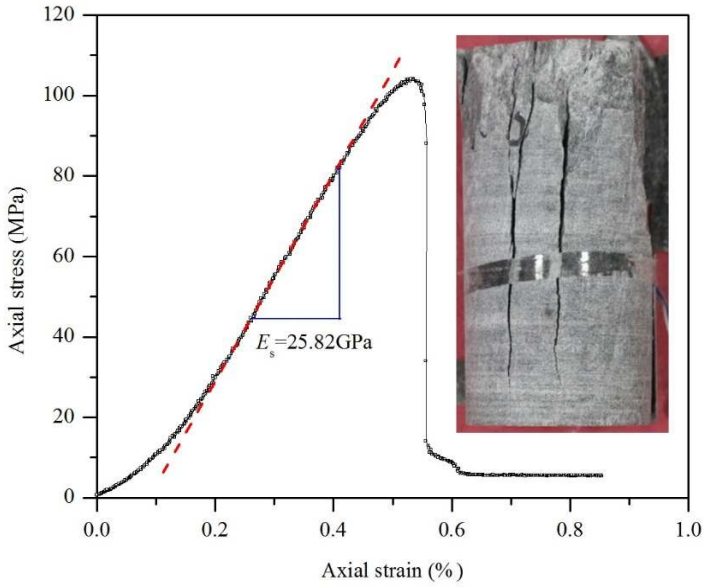

(b) Static uniaxial compressive stress-strain curve and failure mode

Figure 1*: CT images (a) and static mechanical behavior (b) of a typical limestone sample under natural state.*

Table 1: *Physical and static mechanical parameters of a typical limestone sample under natural state.*

Parameter	Symbol	Value	Unit
Bulk density	ρ	2.700	g/cm^3
P-wave velocity	v_p	4351	m/s
Porosity	φ	0.23	%
Uniaxial compressive strength	σ_{ps}	104.14	MPa
Peak strain	ε_{ps}	5.35	10^{-3}
Elastic modulus	E_s	25.82	GPa

Note: Porosity was obtained using the nuclear magnetic resonance test as detailed in §4.4.

2.2 Thermal treatment

To study the effects of thermal treatment on the dynamic mechanical properties of limestone, the test temperature was designed at seven levels: 25°C, 200°C, 300°C, 450°C, 600°C, 750°C, and 900°C. Two environments, the QE and AE, were used for every temperature level except 25°C, resulting in 13 groups with a total of 39 samples prepared, as shown in Table 2.

Table 2: *Physical and dynamic mechanical parameters of limestone samples after thermal treatment.*

T/°C	Sample	ρ/(g/cm^3)	v_p/(m/s)	σ_{pd}/MPa	ε_{pd}/10^{-3}	E_d/GPa
25	A1	2.701	4308	180.4	3.51	78.37
	A2	2.696	4387	187.8	3.61	81.01
	A3	2.702	4359	178.9	3.46	74.15
	Average	2.700	4351	182.4	3.53	77.84
200	B1-v/B1-a	2.701/2.695	3396/3276	174.1/165.6	3.29/3.53	75.64/72.60
	B2-v/B2-a	2.692/2.691	3330/3288	180.2/167.3	3.03/3.84	84.43/67.89
	B3-v/A3-a	2.695/2.697	3321/3363	169.4/176.8	3.98/3.65	69.96/77.53
	Average	2.696/2.694	3352/3309	174.6/169.9	3.43/3.67	76.68/72.67
300	C1-v/C1-a	2.702/2.693	2963/2723	164.0/182.2	4.58/3.57	60.29/78.49
	C2-v/C2-a	2.698/2.688	2917/2716	173.9/176.3	3.42/3.48	76.27/73.13
	C3-v/C3-a	2.695/2.695	2992/2608	174.7/165.7	3.60/4.24	70.25/62.75
	Average	2.698/2.692	2957/2682	170.9/174.7	3.87/3.76	68.93/71.46
450	D1-v/D1-a	2.681/2.679	2315/2146	168.8/141.7	3.85/4.01	68.96/55.83
	D2-v/D2-a	2.687/2.684	2308/2161	159.5/150.6	4.47/4.42	57.10/50.79
	D3-v/D3-a	2.692/2.672	2366/2237	162.3/168.4	3.78/3.87	65.26/67.01
	Average	2.687/2.678	2330/2181	163.5/153.6	4.03/4.10	63.77/57.88
600	E1-v/E1-a	2.667/2.626	2026/1699	107.2/107.7	7.14/6.54	23.72/26.58
	E2-v/E2-a	2.668/2.629	1970/1680	120.9/95.4	6.61/7.47	30.18/21.07
	E3-v/E3-a	2.658/2.640	2061/1791	117.1/102.3	6.25/7.16	29.97/23.15
	Average	2.664/2.632	2019/1723	115.1/101.8	6.67/7.06	27.96/23.60
750	F1-v/F1-a	2.617/2.590	1795/1408	89.0/71.2	8.65/8.55	16.67/13.91
	F2-v/F2-a	2.613/2.599	1792/1489	104.7/74.8	7.74/8.79	22.32/13.44
	F3-v/F3-a	2.627/2.591	1727/1432	101.9/90.3	8.23/8.26	19.81/17.42
	Average	2.619/2.593	1771/1443	98.5/78.8	8.21/8.53	19.60/14.92
900	G1-v/G1-a	2.580/2.518	1456/1233	59.9/39.0	9.37/10.24	10.22/6.21
	G2-v/G2-a	2.587/2.517	1438/1163	70.1/37.9	7.98/11.15	13.03/5.80
	G3-v/G3-a	2.575/2.530	1527/1121	58.4/31.8	9.25/10.39	9.69/5.17
	Average	2.581/2.522	1474/1172	62.8/36.2	8.87/10.59	10.98/5.73

Note: The symbol "-v" means that the sample was heated in the quasi-vacuum environment, while "-a" means that the sample was heated in the air-filled environment.

The thermal treatment was performed using a MXQ1700 box-type furnace (Figure 2a) produced by Shanghai Micro-X Furnace. This device can provide several thermal environments, such as the QE (Figure 2b), AE (Figure 2c), nitrogen atmosphere environment and so on. The air pressure in the QE was below 0.01 MPa throughout the thermal treatment process. Each group was heated at a rate of 5°C/min, which was sufficiently slow to avoid cracking due to thermal shock (Nasseri et al. 2007). The preordained temperature was held constant for 2 hours. Then, the muffle furnace was powered off and samples were left in the furnace to cool to room temperature naturally. Furthermore, samples heated in the QE were sealed using preservative film to provide insulation from the external environment. Figure 2d and Figure 2e show typical samples after thermal treatment. Note that the color of the limestone changes from dark grey (25°C ~ 450°C) to off-white (600°C and 750°C) and white (900°C) with increasing temperature.

The bulk density (ρ) of limestone samples after thermal treatment was determined using the method recommended by the ISRM (Ulusay and Hudson 2007). The mass was measured using an electronic balance with an accuracy of 0.01 g, and the bulk volume was obtained using a vernier caliper with an accuracy of 0.02 mm. Moreover, the P-wave velocity (v_p) was tested using a RSM-SY5 nonmetal ultrasonic detector with a sampling precision of 0.1 μs.



(a) MXQ1700 box-type furnace

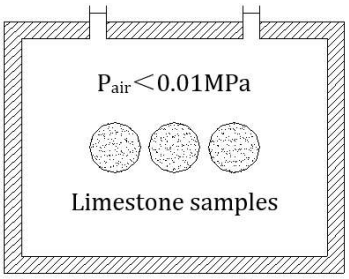

Note: P_{air} represents air pressure

(b) Quasi-vacuum environment

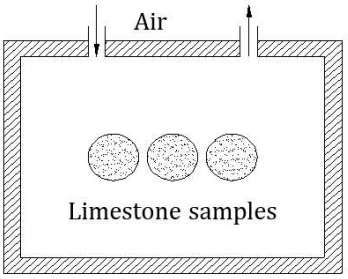

(c) Air-filled environment



(d) Typical limestone samples after thermal treatment in the quasi-vacuum environment

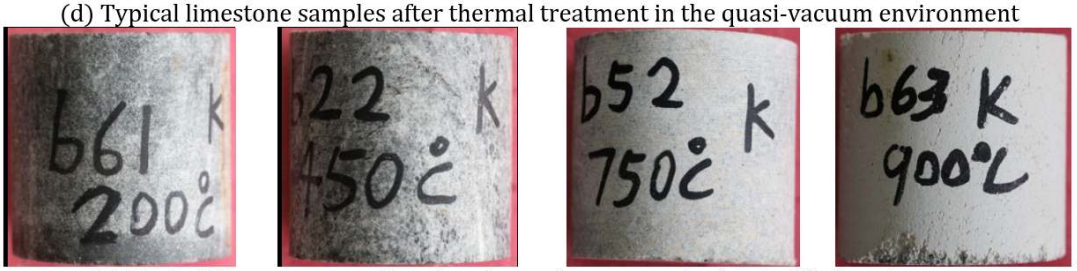

(e) Typical limestone samples after thermal treatment in the air-filled environment

Figure 2: *The high temperature furnace and typical limestone samples after thermal treatment.*

2.3 Dynamic uniaxial compressive test

An SHPB system was employed to conduct the dynamic uniaxial compressive test in this study. This system mainly consists of a gas gun, a striker bar, an incident bar, a transmitted bar, a signal acquisition system (including two strain gauges, a dynamic strain meter and an oscilloscope) and an energy absorption device (Xia and Yao 2015), as shown in Figure 3. A sample is sandwiched between the incident bar and transmitted bar. In our SHPB system, the diameter of all bars is 60 mm, and the lengths of the incident and transmitted bars are 5000 and 3000 mm, respectively. All bars are made from high-strength steel (ASTM9260) with a high yield strength of 1.2 GPa. Strain gauges were glued at 2000 and 1000 mm away from the bar-sample interfaces on the incident and transmitted bars, respectively. A small rubber disc with a 12 mm diameter and 0.2 mm thickness was placed between the striker and incident bar to eliminate the inertia effect inside the sample, i.e., to act as a pulse shaper. The pressure of the gas gun was set to a fixed value of 0.25 MPa to maintain a constant average strain rate for all the samples.

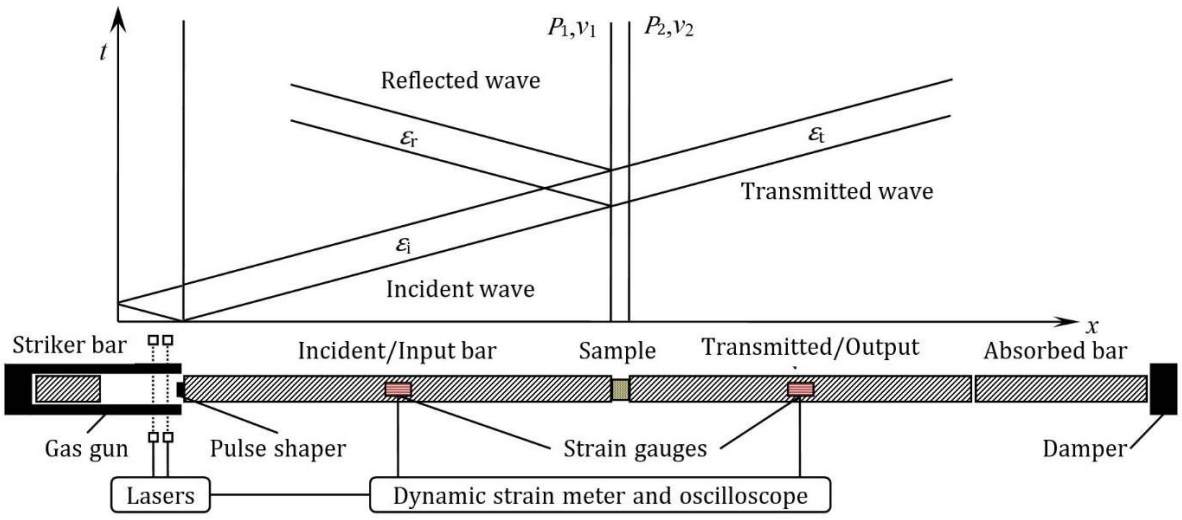

Figure 3: *Schematics of a SHPB system and the x-t diagram of stress waves propagation in SHPB.*

As an example, Figure 4 shows the incident wave (ε_i), reflected wave (ε_r) and transmitted wave (ε_t) obtained from the signal acquisition system for a typical sample. Due to the effects of the pulse shaper, a non-dispersive incident wave was generated with a slow-rising front, and this wave facilitated the dynamic force balance across the sample and constant strain rate during the loading process (Frew et al. 2001, 2002). The loading forces P_1 and P_2 on both ends of the sample induced by the SHPB can be calculated as follows (Kolsky 1949, 1953):

$$P_1 = A_b E_b \left(\varepsilon_{i+} \varepsilon_r\right) \tag{1}$$

$$P_2 = A_b E_b \varepsilon_t \tag{2}$$

where A_b and E_b = 200 GPa were the cross-sectional area and Young's modulus of the bars, respectively. As shown in Figure 4, the forces P_1 and P_2 were almost identical during the dynamic loading process.

Based on assumptions of the one-dimensional stress wave and stress equilibrium state, the strain ($\varepsilon(t)$) and stress ($\sigma(t)$) within the sample during the dynamic compression process can be calculated as follows (Gray, 2000; Xia et al. 2008):

$$\varepsilon(t) = -\frac{2c_b}{L}\int_0^t \varepsilon_r dt \tag{3}$$

$$\sigma(t) = A_b E_b \varepsilon_t / A \tag{4}$$

where c_b = 5160 m/s is the P-wave velocity of the bars and L and A are the initial length and cross-sectional area of the sample, respectively. Then, the dynamic stress-strain curve can be obtained using Equations (3) and (4).

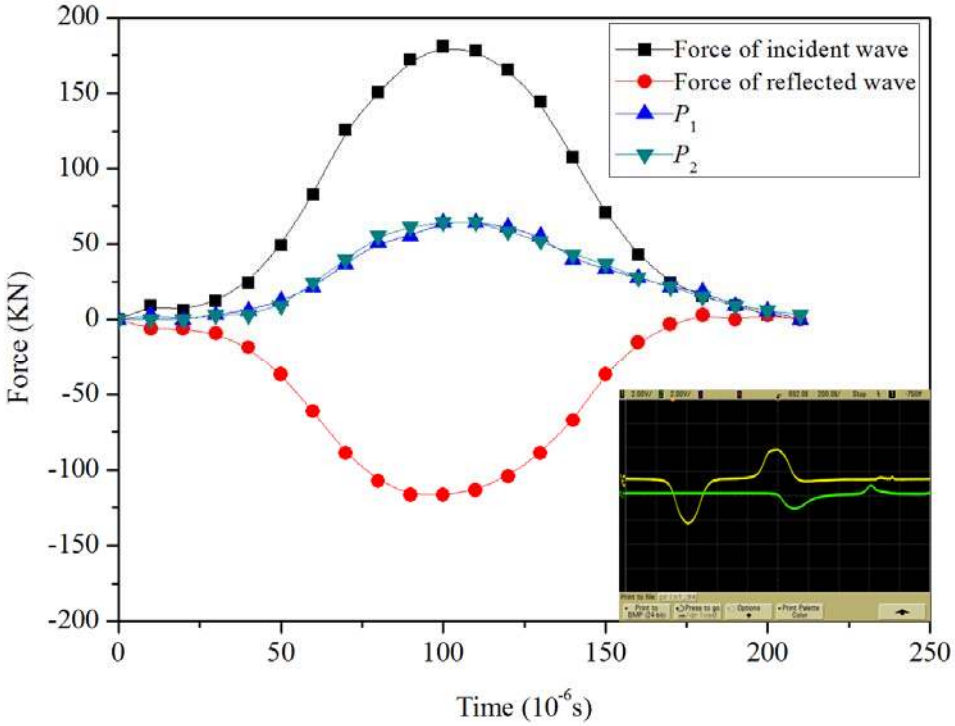

Figure 4: *Dynamic force balance check for a typical sample with pulse shaping.*

As an important parameters in dynamic compressive tests (Zhang and Zhao 2014), the loading rate ($\dot{\sigma}(t)$) can be determined from the time-dependent evolution of $\sigma(t)$. Figure 5 illustrates a typical dynamic compressive loading history, in which a near-linear stage of increasing $\sigma(t)$ can be observed. The slope of this stage is the loading rate, as suggested by the ISRM (Zhou et al. 2012). The strain rate ($\dot{\varepsilon}(t)$) in the test is the average strain rate between the initial moment when stress equilibrium is reached and the failure moment corresponding to the peak load. Then, the dynamic elastic modulus (E_d) can be calculated (Zhou et al. 2012).

$$E_d = \dot{\sigma}(t)/\dot{\varepsilon}(t) \tag{5}$$

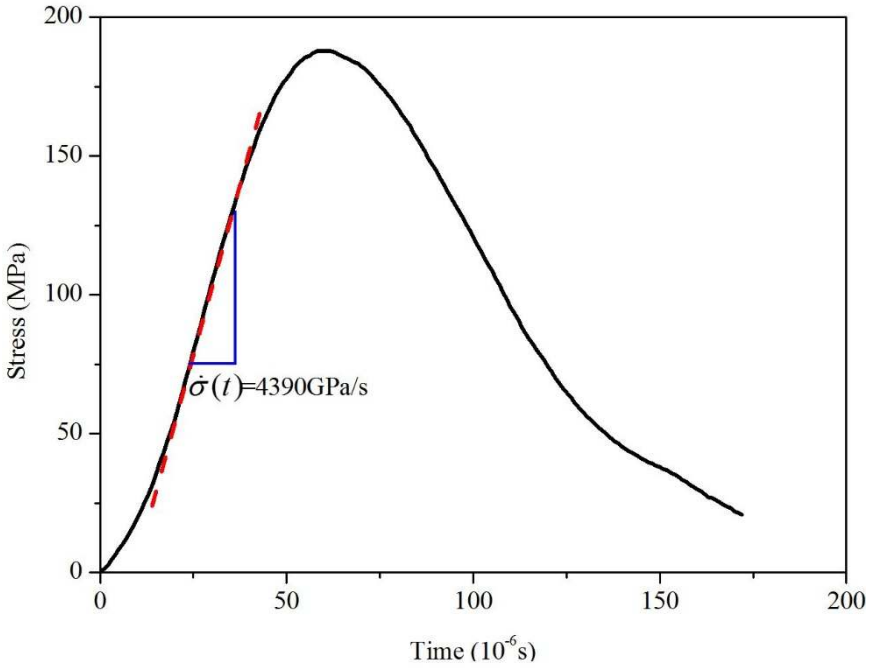

Figure 5: *Determination of the loading rate for a typical SHPB test.*

In all SHPB tests, E_d was calculated using the aforementioned method.

3. RESULTS AND ANALYSIS

3.1 Macro-physical parameters

The bulk density of the limestone samples is 2.700 g/cm^3 at a room temperature of 25°C; however, it varies with increasing temperature, as shown in Table 2 and Figure 6. The average ρ slightly decreases with increasing temperature up to 450°C. Then, a significant reduction (3.94% and 5.83% in QE and AE, respectively) occurs from 450°C to 900°C due to the thermal expansion of minerals, capillary cracks that occur in natural stones and the presence of various materials. These results are similar to those reported in previous studies (Yavuz and Topal. 2007; Ozguven and Ozcelik 2014). Compared to the QE, a more obvious decrease in the average ρ occurs in the AE, especially when the temperature is greater than 450°C. When the temperature increases from 25°C to 900°C, the average ρ decreases by 6.59% in the AE and 4.41% in the QE, respectively.

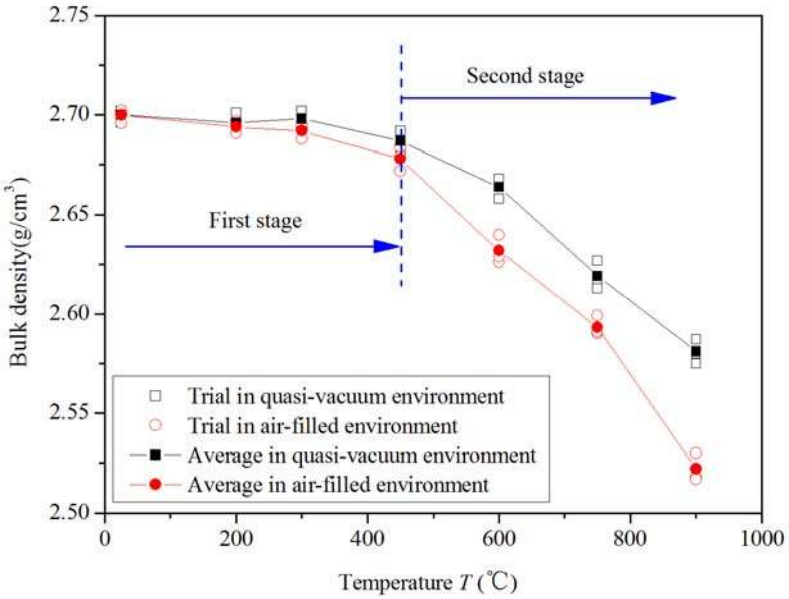

Figure 6: *Variations in the bulk density with varying temperatures from 25°C to 900°C.*

The P-wave velocity of rock is sensitive to microfractures induced by the thermal treatment. The average v_p of limestone is 4351 m/s at 25°C. As shown in Table 2 and Figure 7, a sharp downward trend (>46%) in v_p is observed from 25°C to 450°C; then, a less significant decrease (approximately 20% of the initial value) occurs from 450°C to 900°C. This variation is similar to the results observed in granite analyses (Liu and Xu 2014; Yin et al. 2015). When limestone samples are subjected to a high temperature, protogenic defects such as microcracks and microholes will further expand because of thermal stress or the thermal decomposition of minerals (Yin et al. 2012; Huang and Xia 2015). Therefore, the drastic decrease in v_p (by 66.1% and 73.1% in QE and AE, respectively, at 900°C) is mainly caused by the increase in the pore volume, which produces a barrier effect for P-wave propagation (Nasseri et al. 2007; Heap et al. 2013; Ozguven and Ozcelik 2014). Similar to the ρ of limestone, a greater decrease in v_p can be observed in AE compared to that in QE.

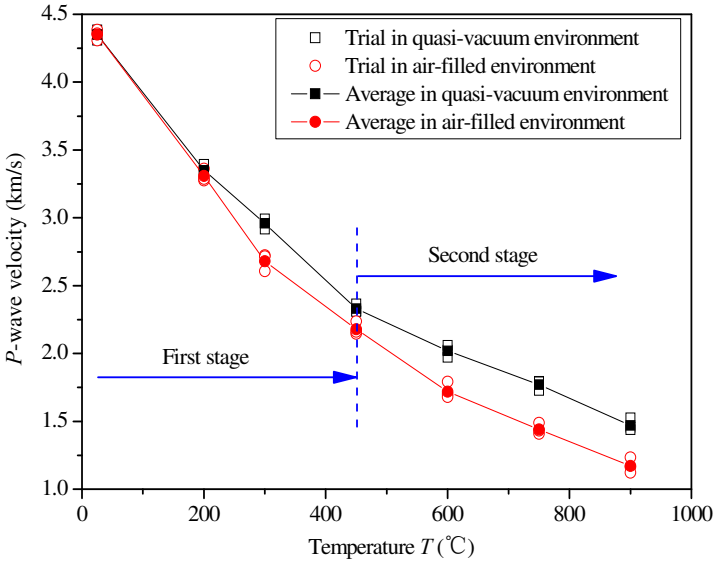

Figure 7: *Variations in the P-wave velocity with varying temperatures from 25°C to 900°C.*

3.2 Dynamic mechanical behaviors

The dynamic stress-strain curves of limestone samples treated at different temperatures are shown in Figure 8. Unlike the static compression results (Figure 1b), the dynamic curves lack the obvious compaction phase and display larger increasing slopes (E_d = 81.01 GPa and E_s = 25.82 GPa for dynamic and static compression, respectively, at 25°C) and higher peak stress (σ_{pd} = 187.8 MPa and σ_{ps} = 104.1 MPa for dynamic and static compression, respectively, at 25°C). Here, E and σ_p are the elastic modulus and peak stress, respectively. These results are mainly due to the much higher loading rate of dynamic compression using the SHPB system and the inherent inertia of internal crystals (Li et al. 2005). Deformation increases with increasing temperature (especially greater than 450°C) in both the QE and AE. A springback in the post-peak region of the stress-strain curves occurs when the temperature is less than 450°C and disappears when the temperature exceeds 450°C. Figure 9 shows the failure characteristics of typical limestone samples after the SHPB test. The size and quantity of rock fragments change distinctly with increasing temperature, and large-diameter fragments are not observed when the temperature exceeds 450°C.

The peak stress (σ_{pd}) of the stress-strain curves, namely, the uniaxial compressive strength in this study, reflects the carrying capacity of limestone, while the peak strain (ε_{pd}) is the strain value corresponding to the peak stress. The variations in σ_{pd} and ε_{pd} in limestone samples after thermal treatment are presented in Table 2 and Figure 10. Slight variations in both σ_{pd} and ε_{pd} occur with increasing temperature up to 450°C regardless of the thermal environment. Then, σ_{pd} displays an obvious decrease (55.2% in the QE and 66.4% in the AE at 900°C), while ε_{pd} exhibits a distinct upward trend (137.1% in the QE and 183.9% in the AE at 900°C). This variation agrees with the results of the static compression of limestone (Ozguven and Ozcelik 2014) and is similar to the dynamic compressive result of biotite granite (Liu and Xu 2014). The limestone loses the majority of its carrying capacity when it is heated to 900°C in both the QE (65.6%) and AE (80.2%).

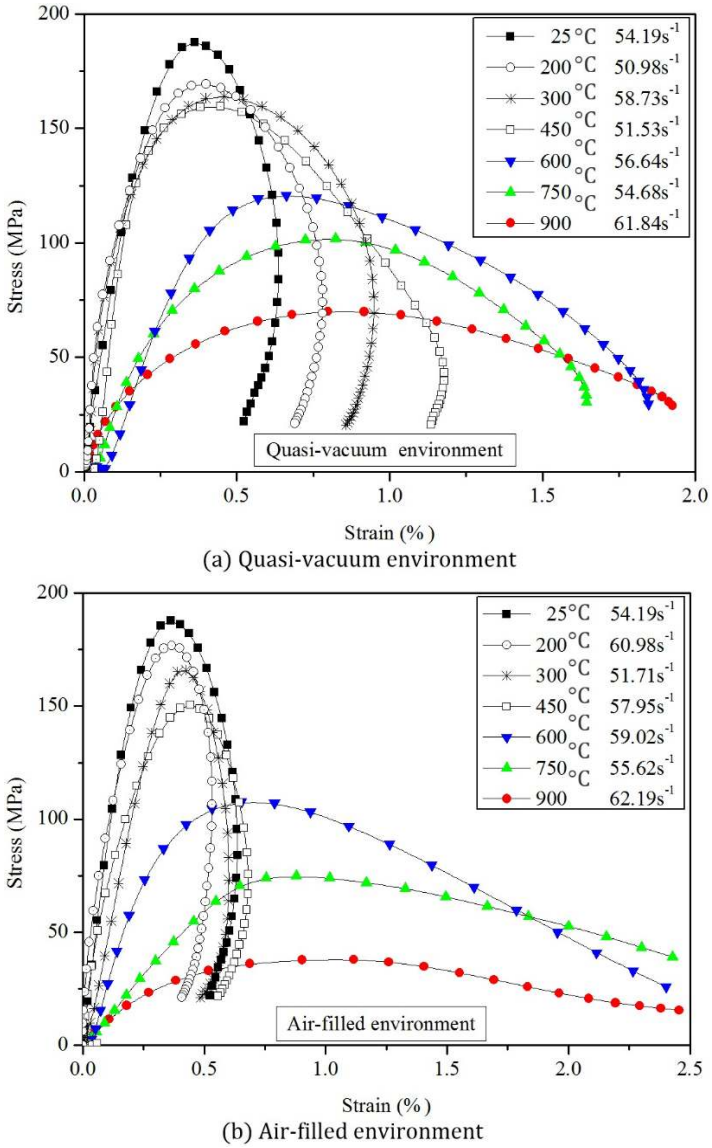

Figure 8: *Dynamic stress-strain curves of typical limestone samples after thermal treatment*

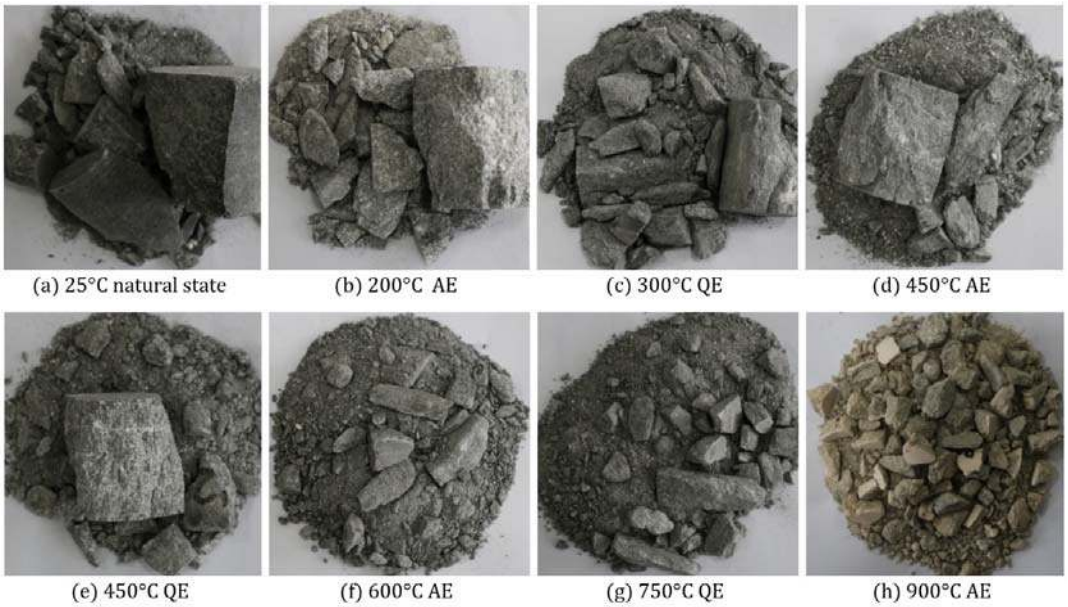

Figure 9: *Failure characteristics of typical limestone samples after the SHPB tests.*

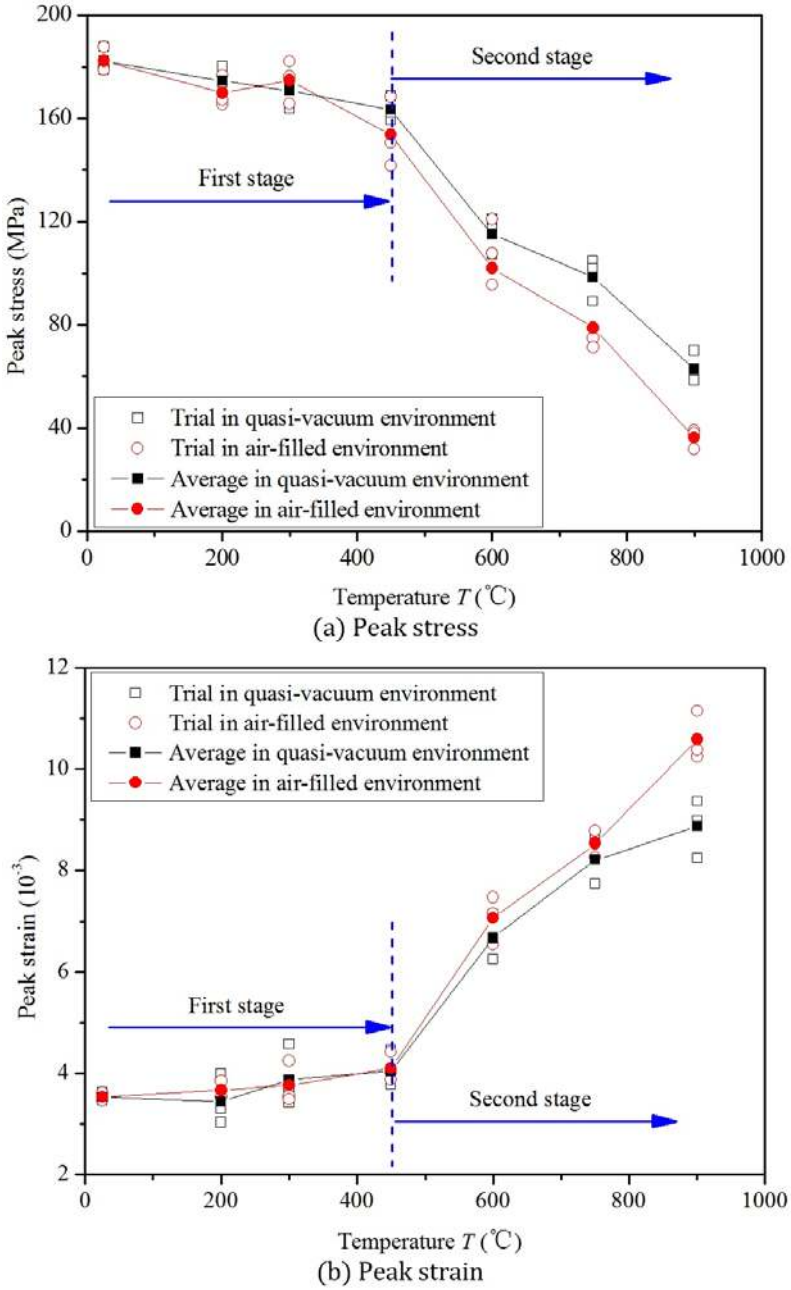

Figure 10: *Variations in the peak stress (a) and peak strain (b) with increasing temperature.*

The elastic modulus is an important index that measures the resistance capacity of elastic deformation. Figure 11 depicts the variation in E_d in relation to temperature, and the detailed results are presented in Table 2. Overall, the E_d of limestone decreases continuously with increasing temperature, and a greater reduction occurs in the AE compared to that in QE (85.9% in the QE and the 92.6% in AE at 900°C). Similar to the peak stress, an evident turning point can be observed at $T = 450$°C during the thermal treatment. The elastic modulus decreases slowly before the turning point (18.1% in the QE and 25.6% in the AE), while a sharp decline occurs after the turning point (67.8% in the QE and 67.0% in the AE).

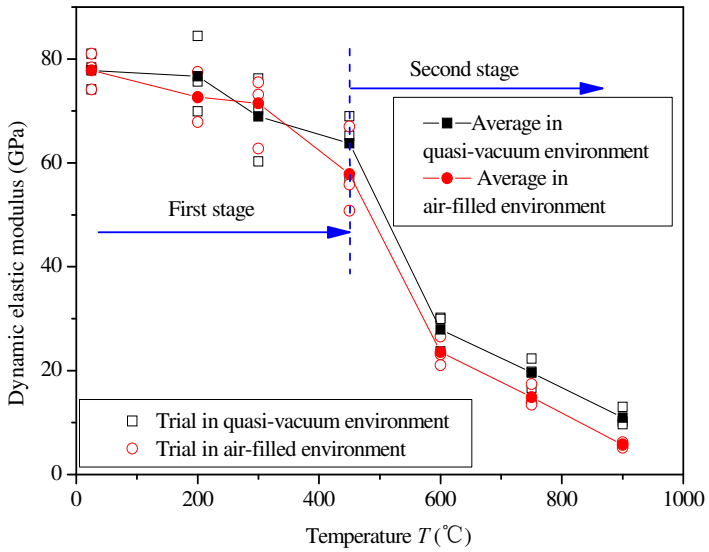

Figure 11: *Variations in the dynamic elastic modulus with increasing temperature.*

4. DISCUSSION

4.1 Stage division during the thermal treatment

Figures 6, 7, 10 and 11 show a concordant turning point $T = 450$°C based on the variations in related parameters with increasing temperature. Parameters such as ρ, v_p, σ_{pd}, ε_{pd} and E_d display different variation trends before and after this critical temperature. To investigate the aforementioned observation, four ratios associated with these parameters are defined:

$$R_{c1} = \left|\alpha_{25} - \alpha_{450}\right| / \alpha_{25} \tag{6}$$

$$R_{c2} = \left|\alpha_{25} - \alpha_{900}\right| / \alpha_{25} \tag{7}$$

$$R_{p1} = \left(\alpha_{25} - \alpha_{450}\right) / \left(\alpha_{25} - \alpha_{900}\right) \tag{8}$$

$$R_{p2} = \left(\alpha_{450} - \alpha_{900}\right) / \left(\alpha_{25} - \alpha_{900}\right) \tag{9}$$

where α is any one of ρ, v_p, σ_{pd}, ε_{pd} and E_d and the subscript of α is the associated temperature of the thermal treatment. The results of these four ratios are listed in Table 3 to clearly illustrate the inflection point. We can divide the temperature range into two stages: the first stage from 25°C to 450°C and the second stage from 450°C to 900°C.

Table 3: *Ratios related to variations of physical and dynamic mechanical parameters.*

Ratio	Bulk density		P-wave velocity		Peak stress		Peak strain		Elastic modulus	
	QE	AE	QE	AE	QE	AE	QE	AE	QE	AE
R_{c1}/%	0.5	0.8	46.4	49.9	10.4	15.8	14.2	16.1	18.1	25.6
R_{c2}/%	4.4	6.6	66.1	73.1	65.6	80.2	151.3	200.0	85.9	92.6
R_{p1}/%	10.9	12.4	70.2	68.3	15.8	19.7	9.4	8.1	21.0	27.7
R_{p1}/%	89.1	87.6	29.8	31.7	84.2	80.3	90.6	91.9	79.0	72.3

4.2 Effect of the environment

When subjected to a high temperature, the transformation from calcite to calcium oxide and the subsequent hydration of calcium oxide induce non-negligible changes in the internal microstructure of limestone. Sufficient water vapor is available for the hydration of calcium oxide in the AE, while hydration is limited in the QE. Therefore, a higher amplitude in the variation of related parameters is generally observed in the AE compared to that in the QE. To determine the effect of environment, the variation in α_{QE}/α_{AE} with increasing temperature is shown in Figure 12. Notably, Figure 12 shows that the ratios of related parameters fluctuate in the first stage and continu-

ously increase in the second stage. Thus, the influence that the environment exerts on the rock properties should not be ignored in engineering practices, especially when the temperature surpasses 450°C.

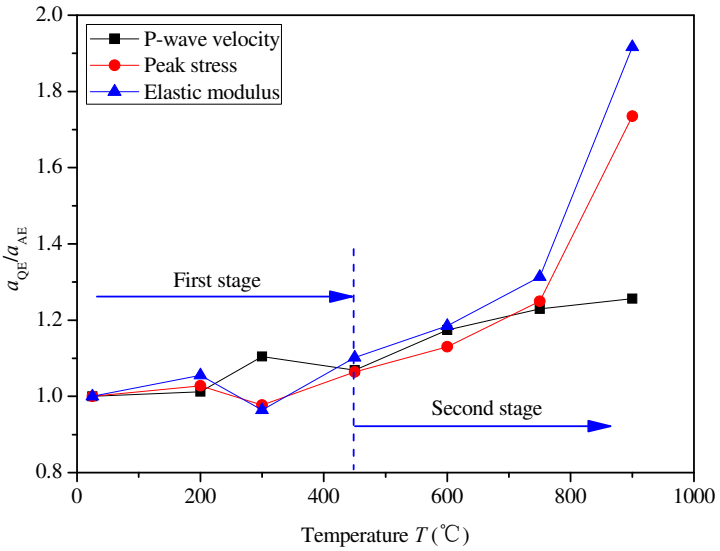

Figure 12: Variations in the ratios of parameters in the QE and AE with increasing temperature.

Note: α_{QE} and α_{AE} represent parameters (the P-wave velocity, peak stress, or elastic modulus) of samples after the thermal treatment in the quasi-vacuum and air-filled environment, respectively.

4.3 Damage factor

Numerous questions regarding the damage properties of rock mass that has undergone deformation and other changes are encountered in rock engineering (Kawamoto et al. 1988; Kachanov, 1993; Hoxha and Homand, 2000; Eslami et al. 2012). Various changes occur in the internal microstructures and mineralogical compositions of rocks after high-temperature exposure, thus altering the propagation path of ultrasonic waves due to refraction and diffraction phenomena. Therefore, the P-wave velocity is sensitive to the thermal treatment, as shown in Figure 7. The damage factor D is introduced and related to v_p as follows (Kawamoto et al. 1988):

$$D = 1 - \left(v_{pt}/v_{pn}\right)^2 \tag{10}$$

where v_{pt} and v_{pn} are the P-wave velocities of samples after thermal treatment and in the natural state (25°C in this study), respectively. Variations in D with temperature are shown in Figure 13. The damage factor continuously increases with increasing temperature. At the critical temperature of T = 450°C, the threshold of D is 0.71 and 0.75 in the QE and AE, respectively. The regression relationships between D and T can be expressed as Langmuir power functions.

$$D = \frac{8.684\times10^{-4}\left(T-25\right)^{1.276}}{1+8.0\times10^{-4}\left(T-25\right)^{1.276}} \qquad R^2 = 0.9969 \text{ for the QE} \tag{11}$$

$$D = \frac{1.607\times10^{-4}\left(T-25\right)^{1.635}}{1+1.6\times10^{-4}\left(T-25\right)^{1.635}} \qquad R^2 = 0.9982 \text{ for the AE} \tag{12}$$

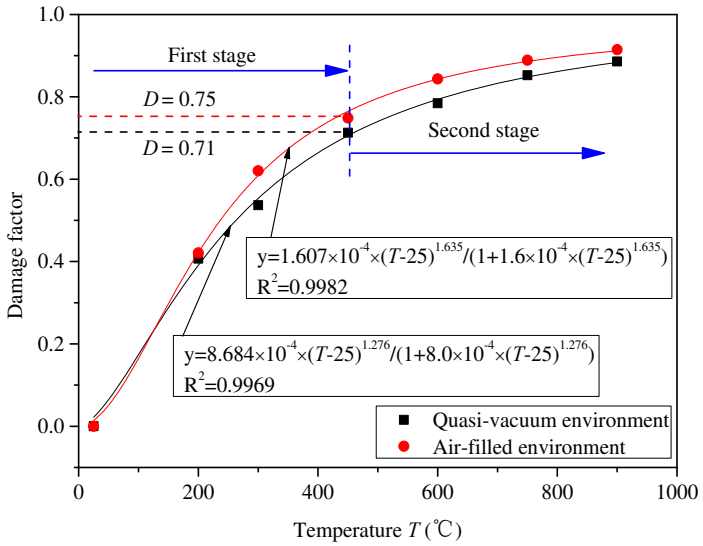

Figure 13: *Variations in the damage factor with increasing temperature.*

4.4 Micromechanisms

Microscopic technologies, including the nuclear magnetic resonance (NMR) test and optical microscopy imaging, are employed to analyze typical limestone samples. NMR is a physical phenomenon in which nuclei in a magnetic field absorb and re-emit electromagnetic radiation (Vandersypen et al. 2001). Low-field NMR technology has been widely used in studies of geological material for more than two decades (Kleinberg et al. 1994; Webber et al. 2013, Kwak et al. 2016). The pore size distributions and NMR images are obtained using a MesoMR23-060H-I NMR system with a resonance frequency of 23.423 MHz, as shown in Table 4. The pore size of limestone falls into four classes based on divisions at 0.1 μm, 1.0 μm and 10.0 μm. In increasing order, these classes are as follows: I-pore, II-pore, III-pore and IV-pore. The brightness of an NMR greyscale image reflects the number of water-filled pores, and a brighter image indicates a larger porosity in the sample. Table 4 also lists the optical microscopic images obtained using a KH-3000 digital microscope with a magnification of 200 times.

Microscopic images provide local intuitive views of limestone in different conditions. A distinct fracture occurs due to the thermal expansion of the sample after a temperature of 450°C is reached, while the apparent color changes slightly compared to that in the natural state. The brightness of the global NMR images indicates that the porosity φ in the sample increases significantly after 450°C is reached (from 0.23% to 1.35% (QE) or 2.36% (AE)). The proportion of IV-pores (>10.0 μm) increases dramatically because of the opening of thermal cracks, especially in the AE (from 5.0% to 69.0%). The thermal decomposition of calcite to calcium oxide plays the most important role in the transformation of the limestone microstructure after 900°C is reached, as shown in Table 4. More bright spots are well distributed in the global NMR image at 900°C, except for the distortions due to paramagnetic material, compared to the image obtained at 450°C. The porosity increases from 1.35% to 4.15% in the QE and from 2.36% to 4.87% in the AE when the temperature increases from 450°C to 900°C, which supports the results of the NMR image analysis. The residual ultrafine particles after thermal decomposition will fill the open thermal fractures to some extent. The proportion of IV-pores (>10.0 μm) decreases from 69.0% to 27.9% in the AE, while the proportion of III-pores (1.0 μm ~ 10.0 μm) increases from 21.9% to 67.9%.

Table 4: *Results of the optical microscopic and NMR tests of limestone samples after thermal treatment.*

State	Optical microscopic image	NMR image	Pore size distribution
25°C	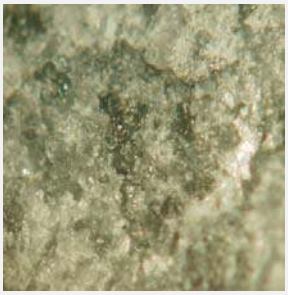 Natural state	 φ=0.23%	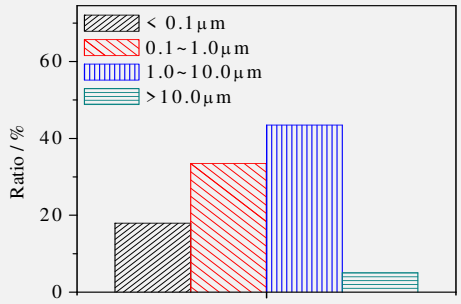
450°C QE	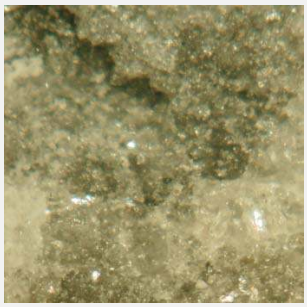 Thermal fracture	 φ=1.35%	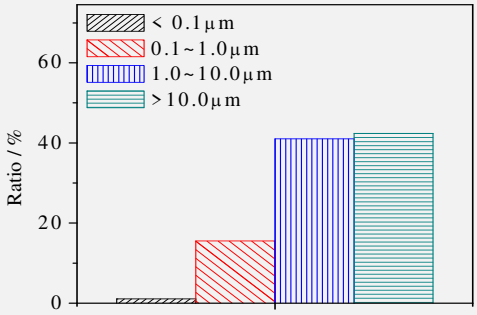
450°C AE	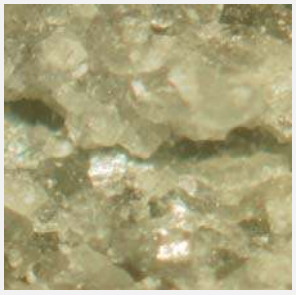 Thermal fracture	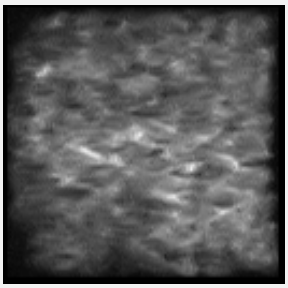 φ=2.36%	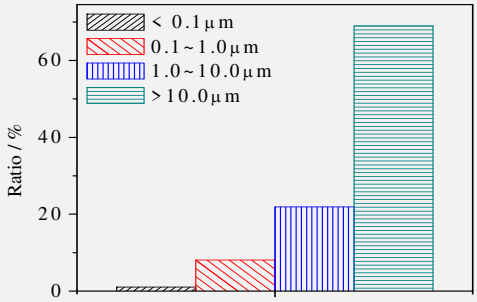
900°C QE	 Thermal decomposition	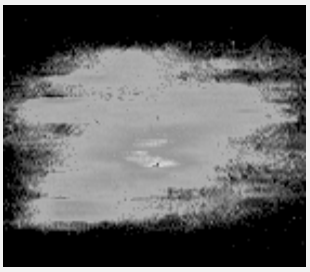 φ=4.15%	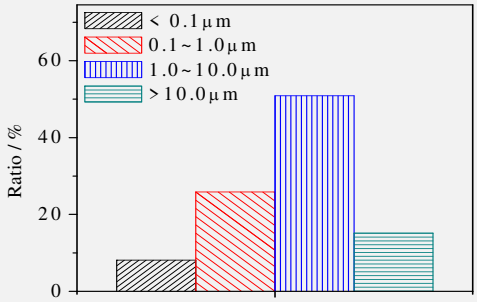
900°C AE	 Thermal decomposition	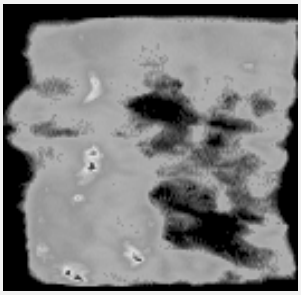 φ=4.87%	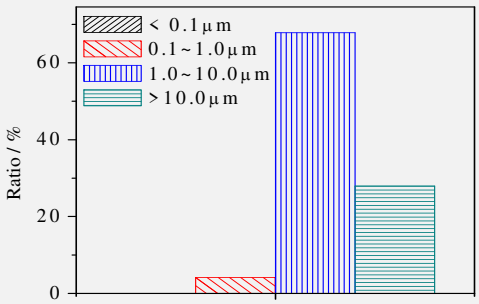

Note: There are image distortions due to paramagnetic material in the last NMR image.

Table 4 shows that in the first stage (25°C ~ 450°C), the thermal damage to the limestone is mainly attributed to volume expansion and crack initiation. Although this transformation of the microstructure leads to a remarkable decrease in the P-wave velocity (see Figure 7), the damage degree is small and does not affect the dynamic bearing capacity (see Figure 10). The difference between related parameters in the QE and the AE is not obvious in this stage (see Figure 12). However, in the second stage (450°C ~ 900°C), the thermal damage to the limestone is primarily caused by mineral decomposition and the hydration of calcium oxide. The limestone sample gradually loses its dynamic bearing and anti-deformation capacities with increasing temperature (see Figures 10 and 11). Additionally, the environment of the thermal treatment has an increasing influence on the dynamic mechanical behavior of the limestone in this stage (see Figure 12).

5 CONCLUSIONS

In this study, a series of laboratory tests, including SHPB, NMR and optical microscopy analyses, are conducted to investigate the influences of the thermal treatment with temperatures ranging from 25°C to 900°C and environments (air-filled environment and quasi-vacuum environment) on the macro-physical and dynamic mechanical properties of limestone. The results show that a critical temperature of 450°C exists, before which and after which the macro-physical and dynamic mechanical properties of limestone exhibit different variations. The thermal damage factor at the critical temperature is 0.71 and 0.75 for the quasi-vacuum and air-filled environment, respectively. In the first stage (25°C ~ 450°C), the thermal damage due to expansion and fracturing slightly influences the related parameters of limestone except the P-wave velocity. However, in the second stage (450°C ~ 900°C), the thermal damage caused by mineral decomposition and hydration leads to a remarkable decrease in the dynamic bearing and anti-deformation capacities. The environment of thermal treatment plays a negligible role in the first stage but an important role in the second stage, and the dynamic compressive strength and modulus of samples in the air-filled environment are much lower than those in the quasi-vacuum environment. The thermal damage should be fully considered in engineering practice associated with limestone, especially when the temperature exceeds 450°C.

Acknowledgment

This study has been partially supported by the Fundamental Research Funds for the Central Universities, China (Grant No. 2017XKQY048).

References

Balme, M. R., Rocchi, V., Jones, C., Sammonds, P. R., Meredith, P. G., & Boon, S. (2004). Fracture toughness measurements on igneous rocks using a high-pressure, high-temperature rock fracture mechanics cell. Journal of Volcanology and Geothermal Research, 132(2), 159-172.

Bhutto, A. W., Bazmi, A. A., & Zahedi, G. (2013). Underground coal gasification: From fundamentals to applications. Progress in Energy and Combustion Science, 39(1), 189-214.

Brotóns, V., Tomás, R., Ivorra, S., & Alarcón, J. C. (2013). Temperature influence on the physical and mechanical properties of a porous rock: San Julian's calcarenite. Engineering Geology, 167, 117-127.

Chaki, S., Takarli, M., & Agbodjan, W. P. (2008). Influence of thermal damage on physical properties of a granite rock: porosity, permeability and ultrasonic wave evolutions. Construction and Building Materials, 22(7), 1456-1461.

Chen, R., Xia, K., Dai, F., Lu, F., & Luo, S. N. (2009). Determination of dynamic fracture parameters using a semi-circular bend technique in split Hopkinson pressure bar testing. Engineering Fracture Mechanics, 76(9), 1268-1276.

Dai, F., Xia, K., & Luo, S. N. (2008). Semicircular bend testing with split Hopkinson pressure bar for measuring dynamic tensile strength of brittle solids. Review of Scientific Instruments, 79(12), 123903.

Dai F, Huang S, Xia KW, Tan ZY (2010) Some fundamental issues in dynamic compression and tension tests of rocks using split hopkinson pressure bar. Rock Mech Rock Eng, 43(6):657-666.

Dai, F., Li, B., Xu, N., Fan, Y., & Zhang, C. (2016a). Deformation forecasting and stability analysis of large-scale underground powerhouse caverns from microseismic monitoring. International Journal of Rock Mechanics and Mining Sciences, 86, 269-281.

Dai, F., Xu, Y., Zhao, T., Xu, N. W., & Liu, Y. (2016b). Loading-rate-dependent progressive fracturing of cracked chevron-notched Brazilian disc specimens in split Hopkinson pressure bar tests. International Journal of Rock Mechanics and Mining Sciences, 88, 49-60.

Dai, F., Li, B., Xu, N., Meng, G., Wu, J., & Fan, Y. (2017). Microseismic Monitoring of the Left Bank Slope at the Baihetan Hydropower Station, China.Rock Mechanics and Rock Engineering, 50(1), 225-232.

David, C., Menéndez, B., & Darot, M. (1999). Influence of stress-induced and thermal cracking on physical properties and microstructure of La Peyratte granite. International Journal of Rock Mechanics and Mining Sciences, 36(4), 433-448.

Eslami, J., Hoxha, D., & Grgic, D. (2012). Estimation of the damage of a porous limestone using continuous wave velocity measurements during uniaxial creep tests. Mechanics of Materials, 49, 51-65.

Ferrero, A. M., & Marini, P. (2001). Experimental studies on the mechanical behaviour of two thermal cracked marbles. Rock mechanics and rock engineering, 34(1), 57-66.

Frew, D. J., Forrestal, M. J., & Chen, W. (2001). A split Hopkinson pressure bar technique to determine compressive stress-strain data for rock materials. Experimental mechanics, 41(1), 40-46.

Frew, D. J., Forrestal, M. J., & Chen, W. (2002). Pulse shaping techniques for testing brittle materials with a split Hopkinson pressure bar. Experimental mechanics, 42(1), 93-106.

Gong, L., Jiang, L., Li, S., Shen, N., Zhang, Y., & Sun, J. (2016). Theoretical and experimental study on longitudinal smoke temperature distribution in tunnel fires. International Journal of Thermal Sciences, 102, 319-328.

Grana, D., & Rossa D E. (2010). Probabilistic petrophysical-properties estimation integrating statistical rock physics with seismic inversion. Geophysics, 75(3), O21-O37.

Gray, G. T. (2000). Classic Split-Hopkinson Pressure Bar Testing. Materials Park, OH: ASM International, 2000. 462-476.

Han, X., He, X., & Cong, B. (2012). The simulation analysis of fire feature on underground substation. In Advances in Future Computer and Control Systems (pp. 659-664). Springer Berlin Heidelberg.

Heap, M. J., Baud, P., & Meredith, P. G. (2009). Influence of temperature on brittle creep in sandstones. Geophysical Research Letters, 36(19).

Heap, M. J., Lavallée, Y., Laumann, A., Hess, K. U., Meredith, P. G., Dingwell, D. B., Huismann, S., & Weise, F. (2013). The influence of thermal-stressing (up to 1000 C) on the physical, mechanical, and chemical properties of siliceous-aggregate, high-strength concrete. Construction and Building Materials, 42, 248-265.

Heuze, F. E. (1983). High-temperature mechanical, physical and thermal properties of granitic rocks — a review. International Journal of Rock Mechanics and Mining Sciences & Geomechanics Abstracts, 20(1), 3-10.

Hoxha, D., & Homand, F. (2000). Microstructural approach in damage modeling. Mechanics of Materials, 32(6), 377-387.

Huang, S., & Xia, K. (2015). Effect of heat-treatment on the dynamic compressive strength of Longyou sandstone. Engineering Geology, 191, 1-7.

Kachanov, M. (1993). Elastic solids with many cracks and related problems. Advances in applied mechanics, 30, 259-445.

Kapusta, K., Stańczyk, K., Wiatowski, M., & Chećko, J. (2013). Environmental aspects of a field-scale underground coal gasification trial in a shallow coal seam at the Experimental Mine Barbara in Poland. Fuel, 113, 196-208.

Kawamoto, T., Ichikawa, Y., & Kyoya, T. (1988). Deformation and fracturing behaviour of discontinuous rock mass and damage mechanics theory. International Journal for Numerical and Analytical Methods in Geomechanics, 12(1), 1-30.

Kleinberg, R. L., Kenyon, W. E., & Mitra, P. P. (1994). Mechanism of NMR relaxation of fluids in rock. Journal of Magnetic Resonance, Series A, 108(2), 206-214.

Koca, M. Y., Ozden, G., Yavuz, A. B., Kincal, C., Onargan, T., & Kucuk, K. (2006). Changes in the engineering properties of marble in fire-exposed columns. International journal of rock mechanics and mining sciences, 43(4), 520-530.

Kolsky, H. (1949). An investigation of the mechanical properties of materials at very high rates of loading. Proceedings of the Physical Society. Section B, 62(11), 676-700.

Kolsky, H. (1953). Stress waves in solids. Oxford, UK: Clarendon Press.

Kwak, H., Hursan, G., Shao, W., Chen, S., Balliet, R., Eid, M., & Guergueb, N. (2016). Predicting Carbonate Rock Properties Using NMR Data and Generalized Interpolation-Based Techniques. Petrophysics, 57(04), 351-368.

Li, M., Mao, X., Cao, L., Pu, H., Mao, R., & Lu, A. (2016) Effects of Thermal Treatment on the Dynamic Mechanical Properties of Coal Measures Sandstone. Rock Mechanics and Rock Engineering, 49:3525-3539.

Li, X. B., Lok, T. S., & Zhao, J. (2005). Dynamic characteristics of granite subjected to intermediate loading rate. Rock Mechanics and Rock Engineering, 38(1), 21-39.

Li, Y. Z., & Ingason, H. (2013). Model scale tunnel fire tests with automatic sprinkler. Fire Safety Journal, 61, 298-313.

Liu, S., & Xu, J. (2014). Mechanical properties of Qinling biotite granite after high temperature treatment. International Journal of Rock Mechanics and Mining Sciences, 71, 188-193.

Nara, Y., Meredith, P. G., Yoneda, T., & Kaneko, K. (2011). Influence of macro-fractures and micro-fractures on permeability and elastic wave velocities in basalt at elevated pressure. Tectonophysics, 503(1), 52-59.

Nasseri, M. H. B., Schubnel, A., & Young, R. P. (2007). Coupled evolutions of fracture toughness and elastic wave velocities at high crack density in thermally treated Westerly granite. International Journal of Rock Mechanics and Mining Sciences, 44(4), 601-616.

Ozguven, A., & Ozcelik, Y. (2014). Effects of high temperature on physico-mechanical properties of Turkish natural building stones. Engineering Geology, 183, 127-136.

Raynaud, S., Fabre, D., Mazerolle, F., Geraud, Y., & Latière, H. J. (1989). Analysis of the internal structure of rocks and characterization of mechanical deformation by a non-destructive method: X-ray tomodensitometry. Tectonophysics, 159(1), 149-159.

Roy, M. P., Singh, P. K., Sarim, M., & Shekhawat, L. S. (2016). Blast design and vibration control at an underground metal mine for the safety of surface structures. International Journal of Rock Mechanics and Mining Sciences, 83, 107-115.

Sengun, N. (2014). Influence of thermal damage on the physical and mechanical properties of carbonate rocks. Arabian Journal of Geosciences, 7(12), 5543-5551.

Ulusay, R., & Hudson, J. A. (2007). The complete ISRM suggested methods for rock characterization, testing and monitoring: 1974-2006. Iskitler Ankara: Kozan Ofset.

Vandersypen, L. M., Steffen, M., Breyta, G., Yannoni, C. S., Sherwood, M. H., & Chuang, I. L. (2001). Experimental realization of Shor's quantum factoring algorithm using nuclear magnetic resonance. Nature, 414(6866), 883-887.

Vinciguerra, S., Trovato, C., Meredith, P. G., & Benson, P. M. (2005). Relating seismic velocities, thermal cracking and permeability in Mt. Etna and Iceland basalts. International Journal of Rock Mechanics and Mining Sciences, 42(7), 900-910.

Wang, Q. Z., Li, W., & Xie, H. P. (2009). Dynamic split tensile test of flattened Brazilian disc of rock with SHPB setup. Mechanics of Materials, 41(3), 252-260.

Wang, Z. L., & Hao, S. (2017). Study on Dynamic Compressive Mechanical Properties and Failure Modes of Heat-Treated Granite. Latin American Journal of Solids and Structures, 14(4), 657-673.

Webber, J. B. W., Corbett, P., Semple, K. T., Ogbonnaya, U., Teel, W. S., Masiello, C. A., Fisher Q. J., Valenza, J. J., Song, Y. Q., & Hu, Q. (2013). An NMR study of porous rock and biochar containing organic material. Microporous and Mesoporous Materials, 178, 94-98.

Xia, K., Rousseau, C. E., & Rosakis, A. (2008). Experimental investigations of spontaneous bimaterial interfacial fractures. Journal of Mechanics of Materials and Structures, 3(1), 173-184.

Xia, K., & Yao, W. (2015). Dynamic rock tests using split Hopkinson (Kolsky) bar system — A review. Journal of Rock Mechanics and Geotechnical Engineering, 7(1), 27-59.

Xu, X. L., Feng, G. A. O., Shen, X. M., & Xie, H. P. (2008). Mechanical characteristics and microcosmic mechanisms of granite under temperature loads. Journal of China University of Mining and Technology, 18(3), 413-417.

Yao, W., Xu, Y., Wang, W., & Kanopolous, P. (2016) Dependence of Dynamic Tensile Strength of Longyou Sandstone on Heat-Treatment Temperature and Loading Rate. Rock Mechanics and Rock Engineering, 49:3899-3915.

Yavuz, A. B., & Topal, T. (2007). Thermal and salt crystallization effects on marble deterioration: examples from Western Anatolia, Turkey. Engineering geology, 90(1), 30-40.

Yin, T., Li, X., Xia, K., & Huang, S. (2012). Effect of thermal treatment on the dynamic fracture toughness of Laurentian granite. Rock mechanics and rock engineering, 45(6), 1087-1094.

Yin, T., Li, X., Cao, W., & Xia, K. (2015). Effects of thermal treatment on tensile strength of Laurentian granite using Brazilian test. Rock Mechanics and Rock Engineering, 48(6), 2213-2223.

Yu, L., Su, H., Jing, H., Zhang, Q., & Yang, E. (2017). Experimental study of the mechanical behavior of sandstone affected by blasting. International Journal of Rock Mechanics and Mining Sciences, 93, 234-241.

Zhang, Q. B., & Zhao, J. (2014). A review of dynamic experimental techniques and mechanical behaviour of rock materials. Rock mechanics and rock engineering, 47(4), 1411-1478.

Zhou, Y. X., Xia, K., Li, X. B., Li, H. B., Ma, G. W., Zhao, J., Zhou Z. L. & Dai, F. (2012). Suggested methods for determining the dynamic strength parameters and mode-I fracture toughness of rock materials. International Journal of Rock Mechanics and Mining Sciences, 49, 105-112.